Supplementary Information

3.4 % solar-to-ammonia efficiency from nitrate using Fe single atomic catalyst supported on MoS_2 nanosheets

Ji Li,[a,b] Yuan Zhang,[a] Chao Liu,[c] Lirong Zheng,[d] Eddy Petit,[b] Kun Qi,[b] Yang Zhang,[b] Huali Wu, [b] Wensen Wang,[b] Antoine Tiberj,[e] Xuechuan Wang,[a] Manish Chhowalla,[f] Luc Lajaunie,[g,h] Ruohan Yu,[i] Damien Voiry [b,*]

[a] *College of Bioresources and Materials Engineering, Shaanxi University of Science & Technology, Xi'an 710021, PR China*

[b] *Institut Europeen des Membranes, IEM, UMR 5635, Université Montpellier, ENSCM, CNRS, 34095 Montpellier Cedex 5, France*

[c] *Shaanxi Collaborative Innovation Center of Industrial Auxiliary Chemistry and Technology, Shaanxi University of Science and Technology, Xi'an 710021, PR China*

[d] *Institute of High Energy Physics, Chinese Academy of Science, Beijing 100049, PR China*

[e] *Laboratoire Charles Coulomb (L2C), Université de Montpellier, CNRS, Montpellier, 34095, France*

[f] *Department of Materials Science & Metallurgy, University of Cambridge, Cambridge, UK*

[g] *Departamento de Ciencia de los Materiales e Ingeniería Metalúrgica y Química Inorgánica, Facultad de Ciencias, Universidad de Cádiz, Campus Río San Pedro S/N, Puerto Real, 11510, Cádiz, Spain*

[h] *Instituto Universitario de Investigación de Microscopía Electrónica y Materiales (IMEYMAT), Facultad de Ciencias, Universidad de Cádiz, Campus Río San Pedro S/N, Puerto Real 11510, Cádiz, Spain*

[i] *Nanostructure Research Centre (NRC), Wuhan University of Technology, Wuhan 430070, PR China*

[*] Corresponding author: Damien. Voiry(damien.voiry@umontpellier.fr)

Materials.

Ammonium tetrathiomolybdate ($(NH_4)_2MoS_4$), iron(III) nitrate nonahydrate ($Fe(NO_3)_3 \cdot 9H_2O$), DMF, salicylic acid (SA), ammonium sulfate ($(NH_4)_2SO_4$), sodium citrate dehydrate, sodium nitroferricyanide dihydrate, sodium hypochlorite solution, HNO_3, HCl, KNO_3, $K^{15}NO_3$, and ^{15}N labeled ammonium chloride ($^{15}NH_4Cl$) were purchased from Sigma-Aldrich (France). All the reagents were used as received without further purification. The commercial carbon cloth (CC, HCP331N,) was purchased from Shanghai Hesen Electric Co. (China). The water used throughout all experiments was purified through a Millipore system.

Synthesis of the MoS_2 catalysts

Preparation of Fe-MoS_2. MoS_2 doped with single atoms of Fe were grown using a hydrothermal method using $(NH_4)_2MoS_4$ and $Fe(NO_3)_3 \cdot 9H_2O$ as precursors for MoS_2 and Fe respectively.[1,2] The loading amount of Fe in Fe-MoS_2 was controlled by adjusting the atomic ratio: Fe/Mo of the $Fe(NO_3)_3 \cdot 9H_2O$ and $(NH_4)_2MoS_4$ reagents. Different ratio values in $Fe(NO_3)_3 \cdot 9H_2O$ and $(NH_4)_2MoS_4$ were investigated: 0/1, 0.025/1, 0.050/1, 0.075/1, to 0.100/1 and the corresponding single-atom catalysts were referred to as Fe-MoS_2-m where m presents the molar Fe/Mo ratio of the reagents. For example, in the case of Fe-MoS_2-75, 30.0 mg of $(NH_4)_2MoS_4$, and 3.5 mg of $Fe(NO_3)_3 \cdot 9H_2O$ were dissolved into 25 mL of DMF. The mixtures were dispersed at room temperature with the aid of ultrasounds for 10 min to achieve a homogeneous and transparent red-brown solution. Then, the mixture solution was transferred into a 50 mL Teflon-lined autoclave. A carbon cloth (CC, 2 cm × 4 cm) was used to conduct support for the nanosheets and was immersed in the DMF solution. The autoclave was

then sealed and maintained at 210 °C for 18 h in an oven. After cooling the reactor to room temperature, Fe-MoS_2-75/CC was washed respectively by deionized water and ethanol (3 × 50 mL) to remove unreacted precursors. The Fe-MoS_2-m samples were dried at 70 °C overnight.

Preparation of M-MoS_2 with M= Ni, Co, and Cu. Co, Ni, Cu-MoS_2/CC, and MoS_2/CC were prepared following the same procedure as for Fe-MoS_2. The molar ratio of M/Mo was fixed to a value of 0.075/1 and $Co(NO_3)_2 \cdot 6H_2O$, $Ni(NO_3)_2 \cdot 6H_2O$, $Cu(NO_3)_2 \cdot 3H_2O$ were used precursors of Co, Ni, and Cu respectively.

Preparation of 2H-MoS_2 and defect-rich MoS_2 (d-MoS_2). MoS_2 and defect-rich MoS_2 (d-MoS_2) nanosheets were prepared following our already-reported strategy.[3,4] 2H-MoS_2 was obtained by annealed the as-growth nanosheets (without Fe) under argon (5.0, Linde) at 800 °C for 1 h (the ramping rate is 10 °C/min). d-MoS_2 was obtained by further annealing 2H MoS_2 under Ar/H_2 (5% Varigon, Linde) under vacuum at 600 °C for 30 min with a 10 °C/min ramping rate.

Preparation of Cu and $Cu_{50}Ni_{50}$. Cu and $Cu_{50}Ni_{50}$ were prepared by electrodeposition according to a previously reported protocol.[5] 20mM of $CuSO_4$ and 20mM of $Ni(NO_3)_2$ as precursors for the Cu and Ni. A gas diffusion layer (GDL, Fuel Cell Store) was used as conducting support. Prior to depositing the catalysts, the GDL was treated with sulfuric acid by sonication for 20 minutes. After acid treatment, the remaining acid was rinsed with deionized water for 5 min three times, and the gas diffusion layer was dried at room temperature.

Catalyst characterizations

Physical characterizations. A Hitachi S-4800 instrument was used for SEM and EDX characterization. The morphology and crystalline structure of Fe-MoS_2 were further characterized using FEI Talos F200X TEM. Aberration-corrected transmission electron microscopy, including high-resolution (scanning) TEM imaging (HR-(S)TEM), energy-dispersive X-ray spectroscopy (EDS) and spatially-resolved electron energy-loss spectroscopy (SR-EELS), was performed using a FEI Titan Cubed Themis microscope which was operated at 80 kV. The Themis is equipped with a double Cs aberration corrector, a monochromator, an X-FEG gun, a super EDS detector, and an Ultra High Resolution Energy Filter (Gatan Quantum ERS) which allows for working in Dual-EELS mode. HR-STEM imaging was performed by using high-angle annular dark-field (HAADF) and annular dark-field (ADF) detectors. SR-EELS spectra were acquired with the monochromator excited allowing an energy resolution of 1.0 eV for an energy dispersion of 0.25 eV/pixel. Powder XRD patterns were recorded using a PANalytical X' pert Pro diffractometer with a Cu Kα source (λ = 0.154178 nm). X-ray photoelectron spectrum (XPS) was performed on a Thermo ESCALAB 250XI using monochromatic Al Kα radiation. All binding energies of the spectra were corrected to the C1s peak at 284.6 eV. The Raman spectra were acquired using an Invia Raman Microscope (Renishaw, United Kingdom) with an excitation of 633 nm. X-ray absorption spectra (XAS) at the Fe K-edges (E_0=7200 eV) were collected in the fluorescence mode at the SAMBA beamline of the SOLEIL synchrotron radiation facility. The ultraviolet-visible (UV-Vis) absorbance spectra were obtained on a UV/Vis/NIR Jasco V570 spectrometer (Tokyo, Japan). Nuclear magnetic resonance (NMR) spectroscopy was performed at 25 °C on a Bruker AVANCE III HD spectrometer operating at a ^{1}H frequency of 600 MHz for isotope labeling experiments.

Electrochemical measurements. The electrochemical properties of the catalysts were

evaluated in three-electrode and two-electrode configurations using a PARSTAT MC potentiostat (AMETEK Inc., USA). The measurements were performed using an H-type reactor with two compartments separated by a Nafion® 117 membrane. Ag/AgCl electrode with a glass frit was used as the reference electrode in the three-electrode configuration, while a 1 × 2 cm^{-2} carbon cloth modified with the MoS_2 catalyst and Pt foil were used as the working electrode and counter electrode, respectively. The electrolyte consisted in a 0.1 M of NaOH + 0.1 M Na_2SO_4 solution with 0.1 M of $NaNO_3$. 100 mL of electrolyte was distributed to the cathode and anode compartment. All potentials were referenced to the reversible hydrogen electrode (RHE) by the equation:

$$E_{RHE} = E_{Ag/AgCl} + 0.197 + 0.059 \times pH.$$

Before the NO_3RR measurements, cyclic voltammetry (CV) was run for 30 cycles at a scan rate of 100mV s^{-1} from 1.023 to -0.997 V in order to activate and stabilize the catalyst. The linear sweep voltammetry (LSV) curves were recorded at a scan rate of 20 mV s^{-1} from 1.023 to -0.997 V vs. RHE. The catalytic performance of each catalyst was then evaluated using LSV and chronoamperometry at increasing overpotentials for 1 h to determine the Faradaic efficiency (FE) for ammonia. AC impedance measurements were performed in a 3-electrode configuration using a VSP potentiostat (BioLogics, France) at an onset potential of -0.5 V vs. RHE. The frequency range was set from 10 0000 Hz to 100 Hz with an AC voltage of 30 mV.

To evaluate the electrochemical specific area, the electrochemical double-layer capacitance (C_{dl}) was determined in a potential window without the Faradaic process at increasing scan rates from 20 to 140 mV s^{-1}.

Solar cell testing. The current-voltage characteristics of the solar panel were recorded

using a dual-source meter unit (Keithley Model 2401B). For the photovoltaic-electrolysis experiments, a GaInAs/Ga(In)As/Ge triple-junction solar cell (HGSC-A100B-2S, Hasunopto, China) was coupled to a 2-electrode H-type cell. A Xenon lamp solar simulator (Oriel LS0106) equipped with a Schott K113 Tempax sunlight filter (Praezisions Glas & Optik GmbH) was used to reproduce an AM1.5G illumination (100 mW cm^{-2}). The current of the system was recorded using a PARSTAT MC potentiostat in chronoamperometry mode with an applied potential of 0.001V. The optical power was measured by an optical power meter (HP 81630, Agilent, USA).

PV-electrolysis measurements. The current-voltage characteristics of the solar panel were recorded using a dual-source meter (Keithley Model 2401). For photocatalysis, a solar panel (4V/350mA, Fuel Cell Store, USA) as a power source tandem with an H-type cell to drive NO_3RR. The light source was a 450 W xenon lamp (Oriel) equipped with a Schott K113 Tempax sunlight filter (Praezisions Glas & Optik GmbH) to match the emission spectrum of the lamp to the AM1.5G standard. The current of the system was recorded by chronoamperometry with applying an 0.001V of external bias for different periods under chopped AM 1.5G illumination. The optical power of the sun was measured by an optical power meter (HP 81630, Agilent, USA).

Determination of the NH_3 concentration *via* colorimetry. The colorimetric determination of the concentration of NH_3 was carried out using UV–vis spectrophotometry and the indophenol blue method.[6] 200 µL aliquots of the electrolyte were collected from the cathode chamber and mixed with 50 µL of 0.75 M NaClO (ρ_{Cl} = 4–4.9)/NaOH. 500 µL of 0.4 M salicylic acid/NaOH (0.32 M) and 50 µL of 1.0% (w/w) $Na_2[Fe(CN)_5NO]\cdot 2H_2O$ solutions were successively added. After 1 hour of reaction, the concentration in ammonia was measured from the absorbance of the solution at λ = 660 nm. The Beer-Lambert law combined with a calibration curve was

used to estimate the concentration of ammonia. The Faradaic efficiency and yield rate in NH_3 were calculated using the following Equations 1 and 2:

$$FE_{NH_3} = 8 \times F \times C_{NH_3} \times V / Q \times 100\% \quad (1)$$

$$R_{\text{Yield rate}} = (C_{NH_3} \times V) / (t \times S) \quad (2)$$

where F is the Faraday's constant (C mol^{-1}), C_{NH_3} is the concentration of NH_3 in the cathode chamber (M), Q is the total charge (C) passing the electrode (*i.e.* current times electrolysis time, t (s)is the electrolysis time, S (cm^2) is the geometric area of the working electrode.

Estimation of the energetic efficiency (EE). The half-cell energy conversion efficiency for the production of NH_3 in the 3-electrode and 2-electrode configuration was calculated from Equation 3:[7]

$$EE_{NH_3} = E° \times FE_{NH_3} / (1.23\text{-}V_{\text{in}}) \quad (3)$$

where $E°$ is the standard potential of the reaction:

$$NO_3^- + 4H_2O \rightarrow OH^- + 2O_2 + NH_3, E° = 0.54\text{V}$$

FE_{NH_3} is the faradaic efficiency for NH_3, and V_{in} is the applied voltage on the cell of the 3 or 2-electrode configuration system.

Electric power consumption estimation. The electric power consumption (EPC) for the 2-electrode configuration represents the amount of electric energy (typically expressed in kWh) that is required for producing 1 kg of product, was calculated for NO_3RR by Equation 4:[8]

$$\text{EPC} = V_{\text{in}} \times n \times F / (\text{FE} \times \text{M}) \quad (4)$$

where n is the number of transferred electrons (n = 8 for electrochemical reduction of

173 NO_3^- to NH_3), M is the molecular weight of NH_3.

174 **Estimation of the solar-to-Ammonia (STA) conversion efficiency.** The solar-to-
175 ammonia conversion efficiency for the PV-driven electrolysis of nitrate was calculated
176 by equation 5:[9]

177 $$\mathrm{STA} = (1.23\text{-}E^{\circ}_{NO3/NH3}) \times I_{\mathrm{op}} \times FE_{NH_3} / P_{\mathrm{sun}} \qquad (5)$$

178 where P_{sun} is the power of the sun (100 mW cm^{-2}), I_{op} is the current, $E^{\circ}_{NO3/NH3}$ is the
179 standard potential (0.69 V *vs*. RHE, pH =14).[5]

180 **Computational details.** All the spin-polarized density functional theory (DFT)
181 calculations were implemented in the Vienna Ab-initio Simulation Package (VASP)
182 code with a projector augmented-wave (PAW) method.[10,11] The exchange-correction
183 energy was described using a generalized gradient approximation (GGA) with a
184 Perdew–Burke–Ernzerhof (PBE) format. A plane-wave basis with a kinetic energy
185 cutoff of 520 eV was chosen to expand the electronic wave functions. For M-MoS_2
186 (with M=Fe, Co, Ni, and Cu) model, we chose a 4×4×1 supercell of monolayer MoS_2
187 with a 20 Å vacuum layer above the basal plane and then placed one M atom on Mo
188 topsite as previously described.[12] For MoS_2 M- MoS_2, the (100) surface of MoS_2 was
189 chosen as the active surface for catalysis because the basal plane was considered to be
190 chemically inert according to previous results from the literature. The $(10\bar{1}0)$ edge (i.e
191 Mo-edge) was employed to simulate the NO_3RR performance on MoS_2 and Fe-doped
192 MoS_2. All the structures were allowed to fully relax to the ground state with the
193 convergence of the energy and the forces to 1.0×10^{-5} eV and 0.01 eV $Å^{-1}$. A 3 × 3 × 1
194 Γ-centered Monkhorst-Pack schemed *k*-mesh was used to sample the first Brillouin
195 zone. The DFT-D2 of Grimme was used for the long-range dispersion correction.[13] To
196 evaluate the NO_3RR performance on each catalyst, the considered chemical reactions

can be summarized as shown below (Equations 6-12).

$$* + NO_3^- \rightarrow *NO_3^- \quad (6)$$

$$*NO_3^- + 2H^+ + 2e^- \rightarrow *NO_2 + H_2O \quad (7)$$

$$*NO_2 + 2H^+ + 2e^- \rightarrow *NO + H_2O \quad (8)$$

$$*NO + 2H^+ + 2e^- \rightarrow *N + H_2O \quad (9)$$

$$*N + H^+ + e^- \rightarrow *NH \quad (10)$$

$$*NH + H^+ + e^- \rightarrow *NH_2 \quad (11)$$

$$*NH_2 + H^+ + e^- \rightarrow *NH_3 \quad (12)$$

The Gibbs free energy change (ΔG) of the above-mentioned elementary steps was calculated by Equation 13 based on the computational hydrogen electrode (CHE) model proposed by Nørskov et al.[14]

$$\Delta G = \Delta E + \Delta E_{ZPE} - T\Delta S \quad (13)$$

where ΔE is the energy difference before and after adsorption for each elementary step. ΔE_{ZPE} and ΔS, respectively, the difference of the zero-point energy and the vibrational entropy. All data are listed in Supplementary Table 4. T is the temperature (i.e 298.15 K).

XAS analysis

The acquired EXAFS data were processed according to the standard procedures using the ATHENA module implemented in the IFEFFIT software packages.[15] The k3-weighted EXAFS spectra were obtained by subtracting the post-edge background from the overall absorption and then normalizing for the edge-jump step. Subsequently, k3-weighted χ(k) data of Fe K-edge were Fourier transformed to real (R) space using a Hanning window (dk=1.0 $Å^{-1}$) to separate the EXAFS contributions from

different coordination shells. To obtain the quantitative structural parameters around central atoms, least-squares curve parameter fitting was performed using the ARTEMIS module of IFEFFIT software packages.[16,17]

DFT analysis

The BEP relation describes a law with a linear relationship between the adsorption energy of reactant and the reaction energy barrier on the catalyst surface.[18,19] The BEP relation describes the relationship between the adsorption energy of the reactant and the catalytic reaction energy barrier on the active sites, that is, the catalyst with strong reactant adsorption has a low reaction energy barrier, but the product is difficult to desorb. On the contrary, the reaction would be difficult to occur on the catalyst which possesses weak adsorption for reactant, even though the product is facile to desorb from the catalyst. Although it is essential nature for an excellent catalyst with moderate adsorption energy. Here, the Fe-MoS_2 can powerfully reduce the reaction energy barrier of the NO3RR (i.e. *NO-->*N) due to the strongest adsorption for NO among four SACs.

Supplementary Figures

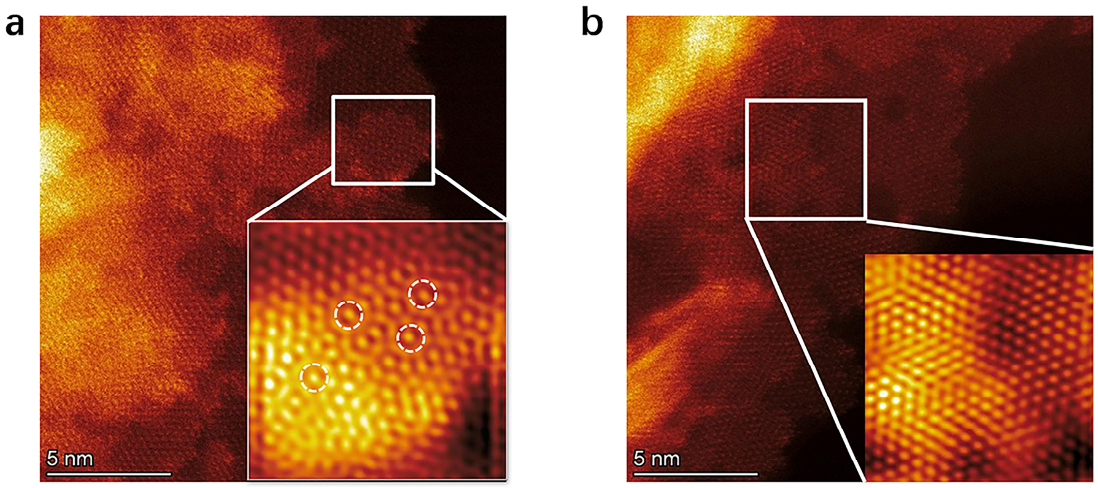

Supplementary Figure 1. High-angle annular dark-field scanning transmission electron microscope (HAADF-STEM) images of Fe-MoS_2 (**a**) and MoS_2 (**b**) nanosheets (inset: the corresponding inverse FFT image).

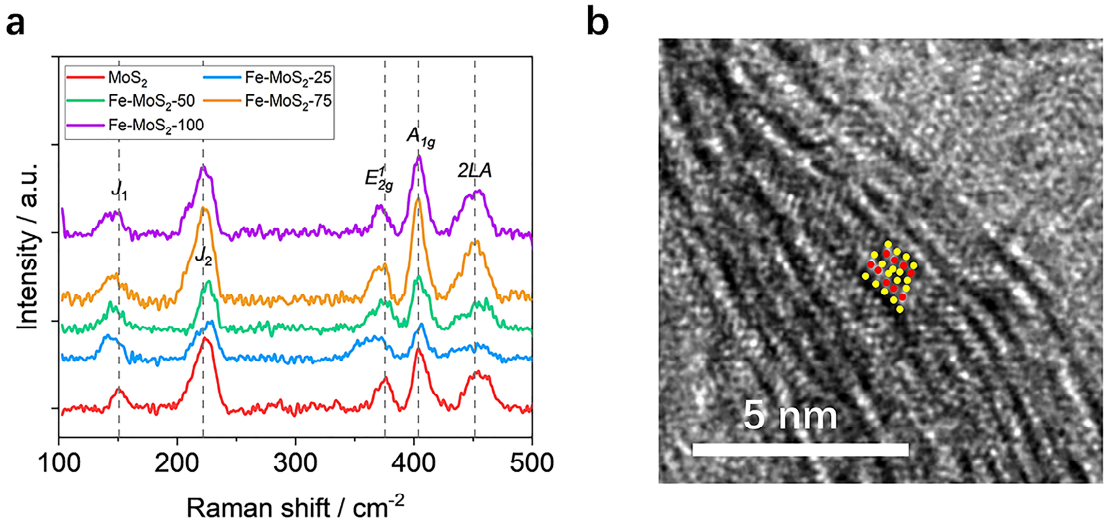

241

242 **Supplementary Figure 2. a**, Raman spectra of the Fe-MoS_2 and MoS_2 nanosheets. **b**,

243 HRTEM of Fe-MoS_2 nanosheets.

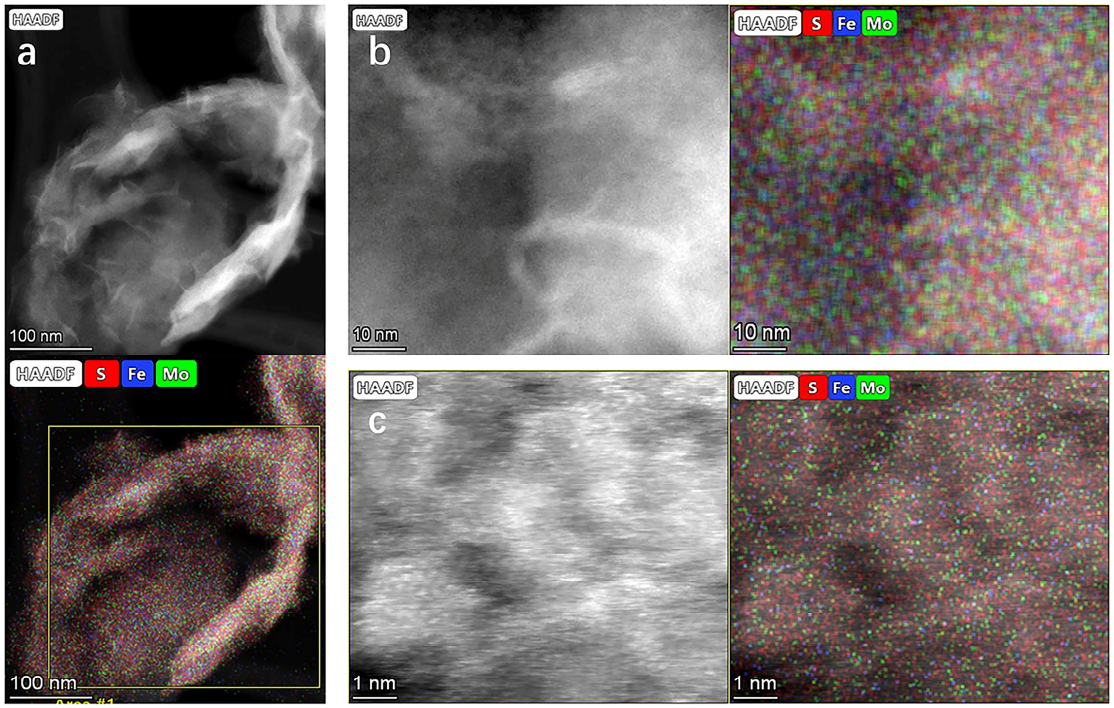

Supplementary Figure 3. High-angle annular dark-field imaging scanning transmission electron microscopy (HAADF-STEM) image of Fe-MoS_2 nanosheets and corresponding high-resolution TEM (HRTEM) – energy dispersive X-ray analyses (EDX), scale bar = 100 nm (**a**), 10 nm (**b**), and 1nm (**c**).

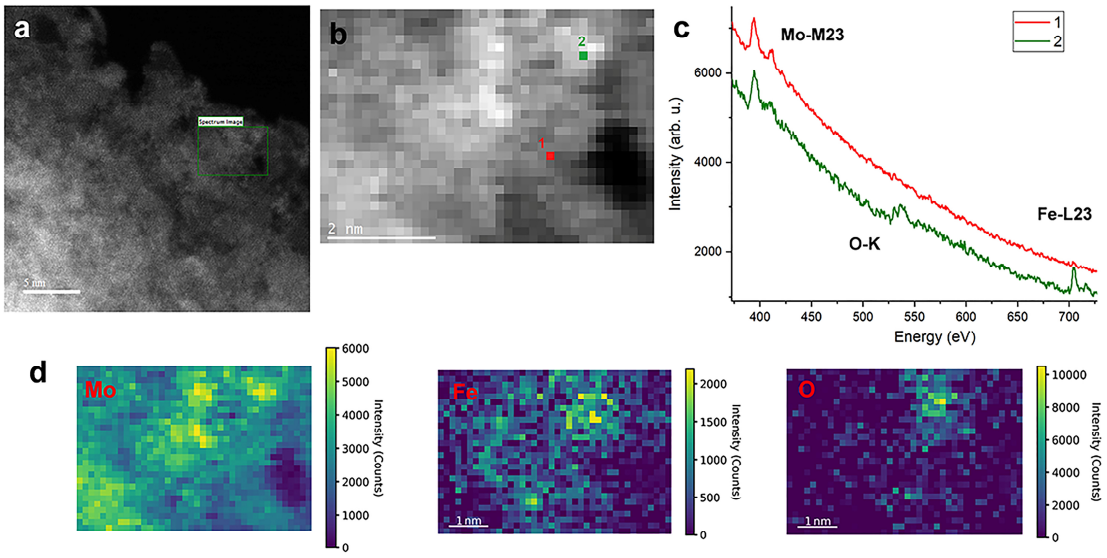

Supplementary Figure 4. EELS analysis of Fe-MoS_2. a, ADF image. The green square highlights the area used to acquire the EELS spectrum image. **b,** ADF image acquired simultaneously as the EELS dataset. The green and red voxels highlight the areas used to extract the EELS spectra shown in c. **c,** Corresponding EELS spectra. **d,** Corresponding EELS chemical maps. The voxel size is below 0.16 nm.

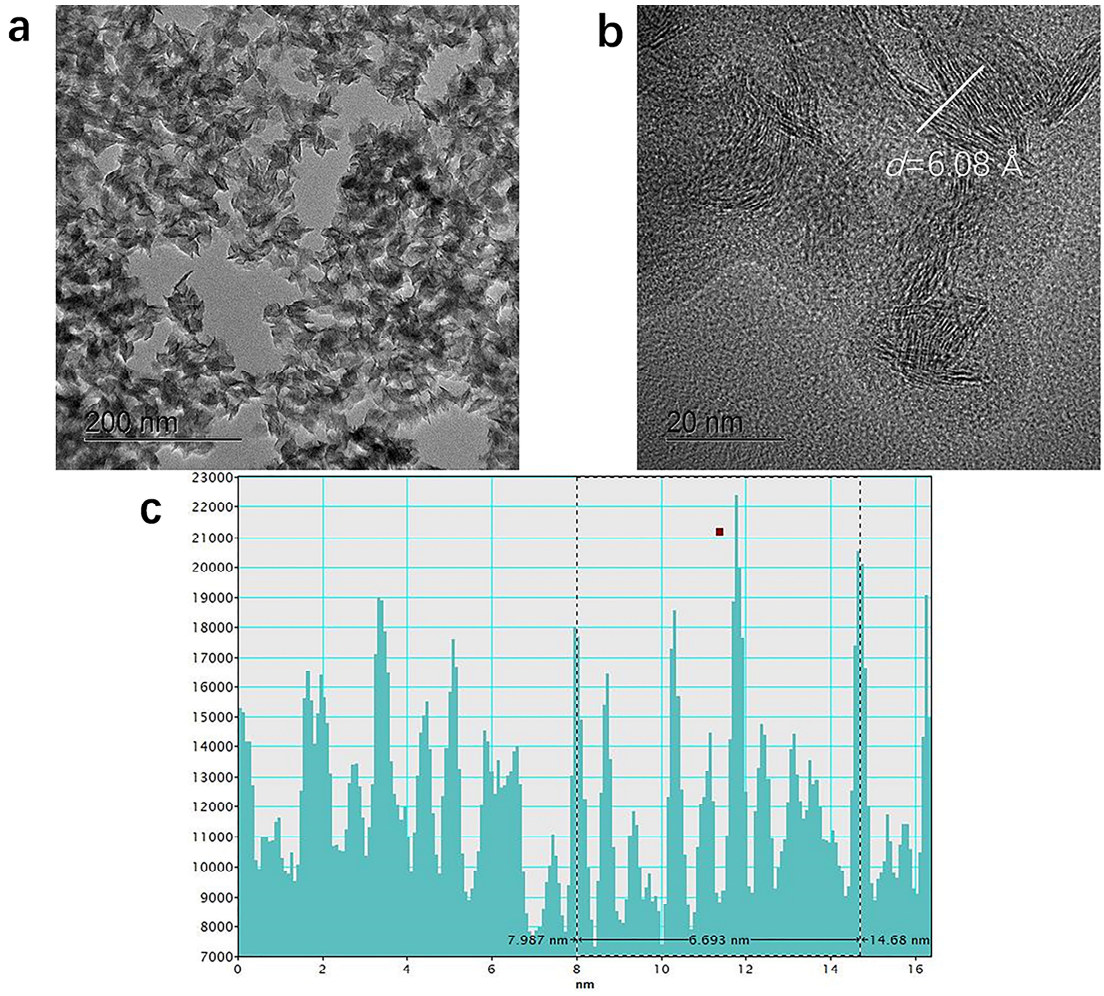

Supplementary Figure 5. TEM (**a**) and HRTEM (**b**) images of pristine MoS_2 nanosheets, respectively. **c**, The line profiles across the pristine layers observed under HRTEM showing an average d-spacing of 6.08 Å.

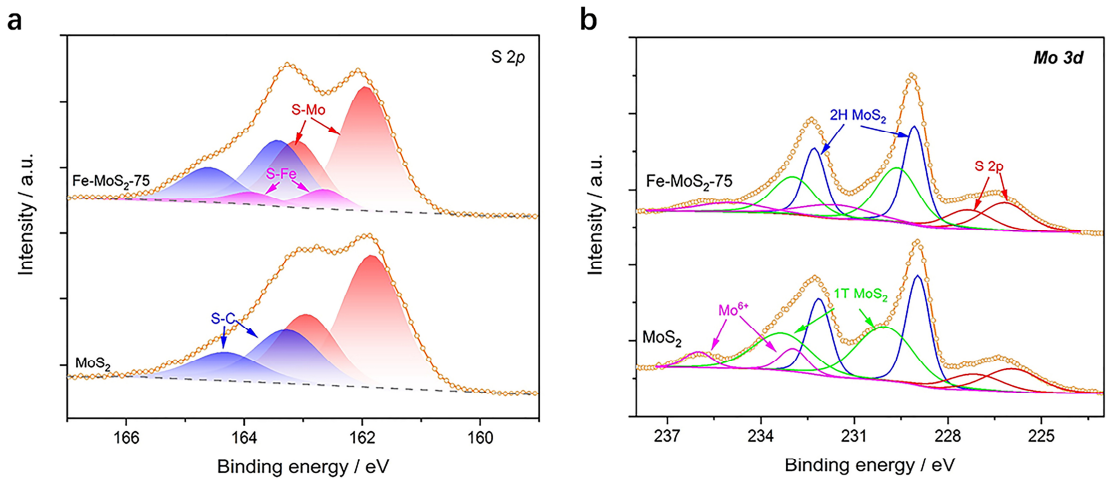

Supplementary Figure 6. X-ray photoelectron spectroscopy (XPS) spectra of S 2p (**a**), and Mo 3d (**b**) for MoS_2 and Fe-MoS_2 nanosheets.

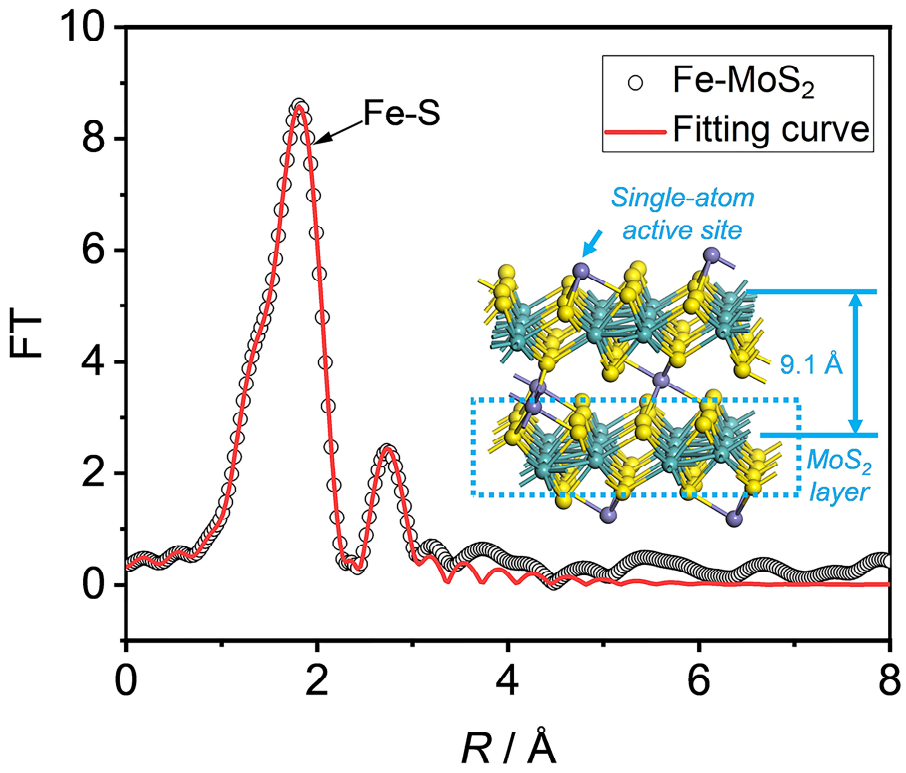

264

265 **Supplementary Figure 7.** Fitting results of Fe-MoS_2 nanosheets, inset its possible

266 structure.

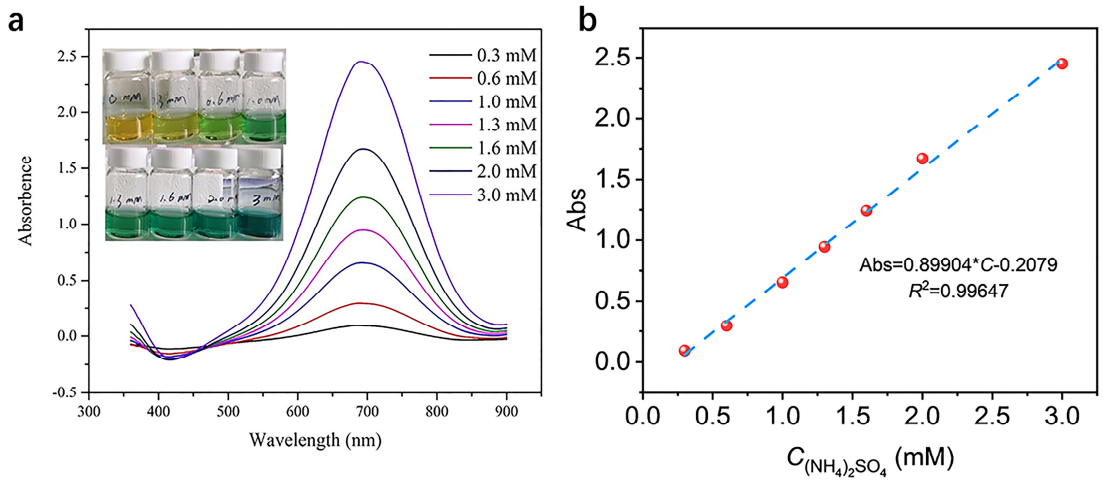

Supplementary Figure 8. a, Photographe of the standard solutions used of the calibration curves presented in Supplementary Figure 8b and corresponding UV-visible absorption spectra. **b**, Calibration curve of NH_4^+ ions present in the standard solutions. The absorbance at 654.5 nm corresponding to the peak of the ammonia was measured to estimate the ammonia concentration in the solutions The calibration curve showed a strictly linear relationship between absorbance and the NH_4^+ concentration over a large range of concentration from 0.3 to 3.0 mM. The ammonia concentration can be estimated using Equation 14:

$$\text{Abs} = 0.0.89904 \times [NH_4^+] + 0.2079, R^2 = 0.99647) \qquad (14)$$

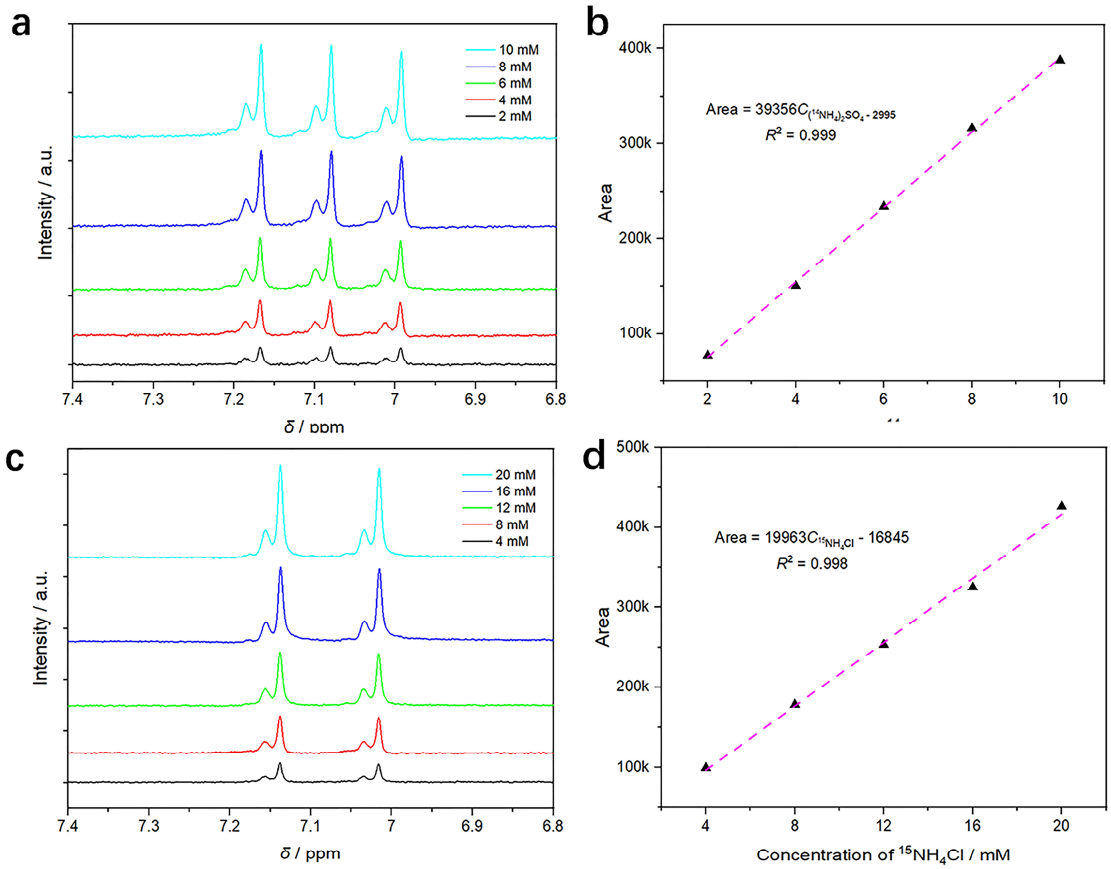

279

280 **Supplementary Figure 9. a**, ^{1}H-NMR spectra of $(^{14}NH_4)_2SO_4$ standard solution at
281 increasing concentrations in the range of 2-10 mM. **b**, Corresponding calibration curve
282 obtained from the integration of the NMR signals. **c**, ^{1}H-NMR spectra of $^{15}NH_4Cl$
283 standard solution at increasing concentrations in the range of 2-10 mM. **d**,
284 Corresponding calibration curve obtained from the integration of the NMR signals.

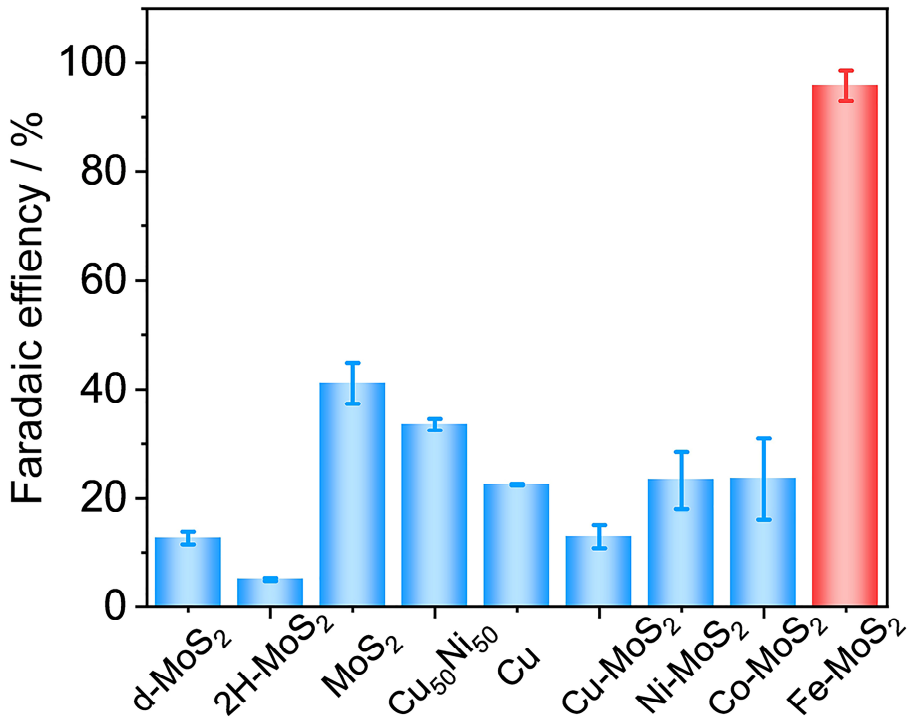

Supplementary Figure 10. a, The Faradaic efficiency of NH_3 of various catalysts under a potential of -0.48 V versus RHE. Among the tested catalysts, d-, 2H-, Co- and Ni-, and Cu-MoS_2 nanosheets exhibited catalytic activities for the reduction of NO_3^- into NH_3 much lower than that of the Fe-MoS_2 nanosheets.

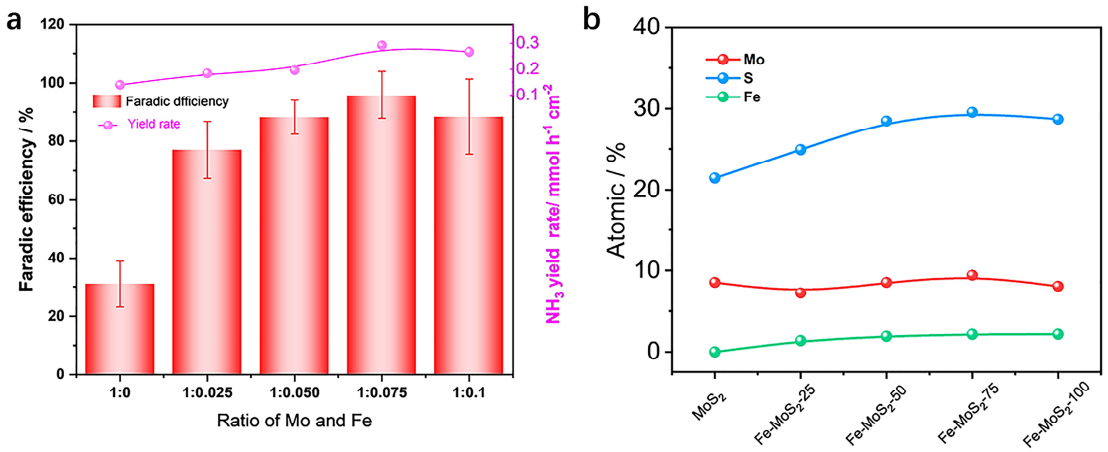

290

291 **Supplementary Figure 11. a**, Influence of the Mo/Fe molar ratio in the Fe-MoS_2-m

292 catalysts on the Faradaic efficiency for ammonia. The measurements were carried out

293 in a 0.1 M electrolyte solution at an applied potential of -0.48 V *versus* the reversible

294 hydrogen electrode (*vs*. RHE). **b**, The atomic percentage of Fe-MoS_2-m catalysts

295 determined by XPS.

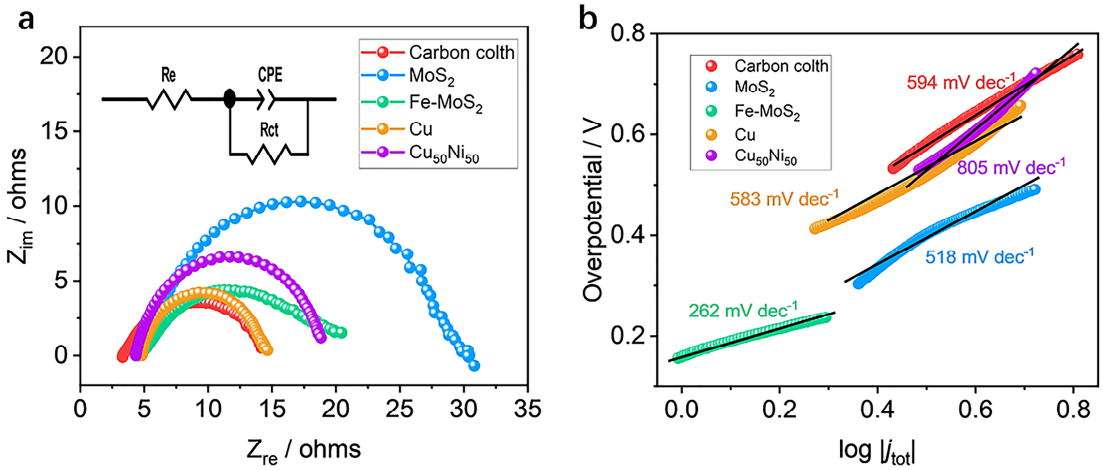

296

297 **Supplementary Figure 12. a,** Nyquist plots for Fe-MoS_2 nanosheets, MoS_2 nanosheets,

298 Cu, $Cu_{50}Ni_{50}$, and carbon cloth. The EIS was performed at an onset potential of -0.5 V

299 vs. RHE from 100 000 Hz and 100 Hz. **b**, Tafel plots of Fe-MoS_2 nanosheets for the

300 NO_3RR, compared with MoS_2 nanosheets, Cu, $Cu_{50}Ni_{50}$, and carbon cloth.

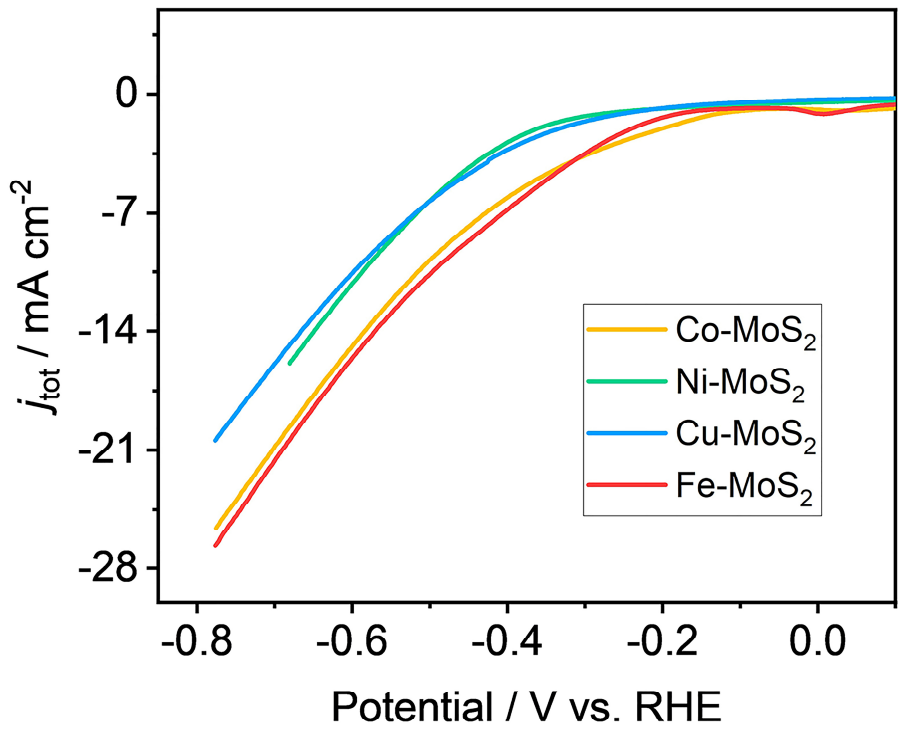

Supplementary Figure 13. Linear scanning voltammetry (LSV) curves for Co-MoS_2 (yellow), Ni-MoS_2 (green), and Cu-MoS_2 (blue), and Fe-MoS_2 nanosheets (red) measured in the presence of 0.1 M $NaNO_3$ electrolyte.

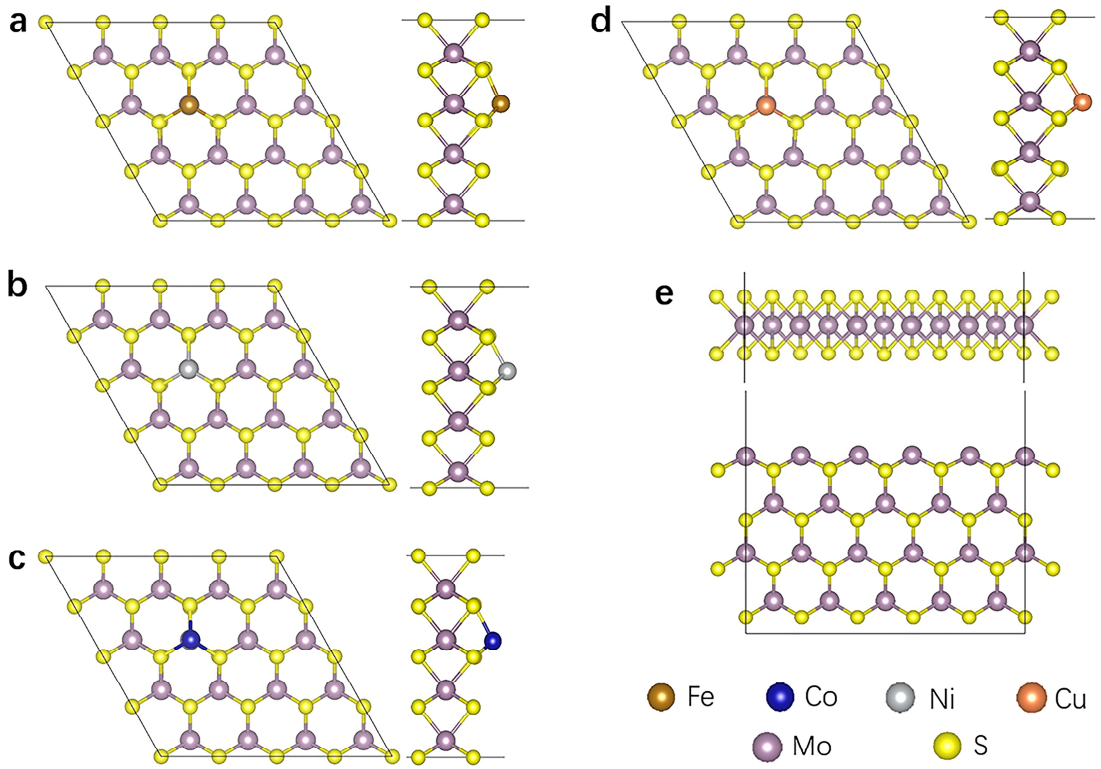

Supplementary Figure 14. Top and side views of various transition metals supported on MoS_2 nanosheets (**a** Fe-MoS_2, **b** Ni-MoS_2, **c** Co-MoS_2, and **d** Cu-MoS_2). Pristine structure for MoS_2 is shown in (e). The color code used for the different elements is as follows: Fe (brown), Mo (violet), S (yellow), Co (blue), Cu (orange), and Ni (grey).

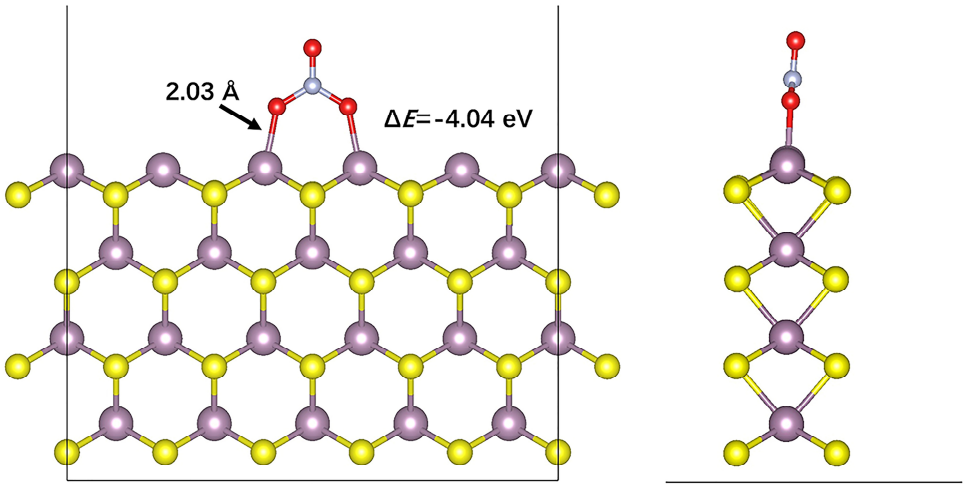

Supplementary Figure 15. Top and side views of the structure of NO_3^- adsorbed on the edge of MoS_2 edge. The color code used of the different elements is as follows: Mo (violet), S (yellow), O (red), N (light blue), respectively.

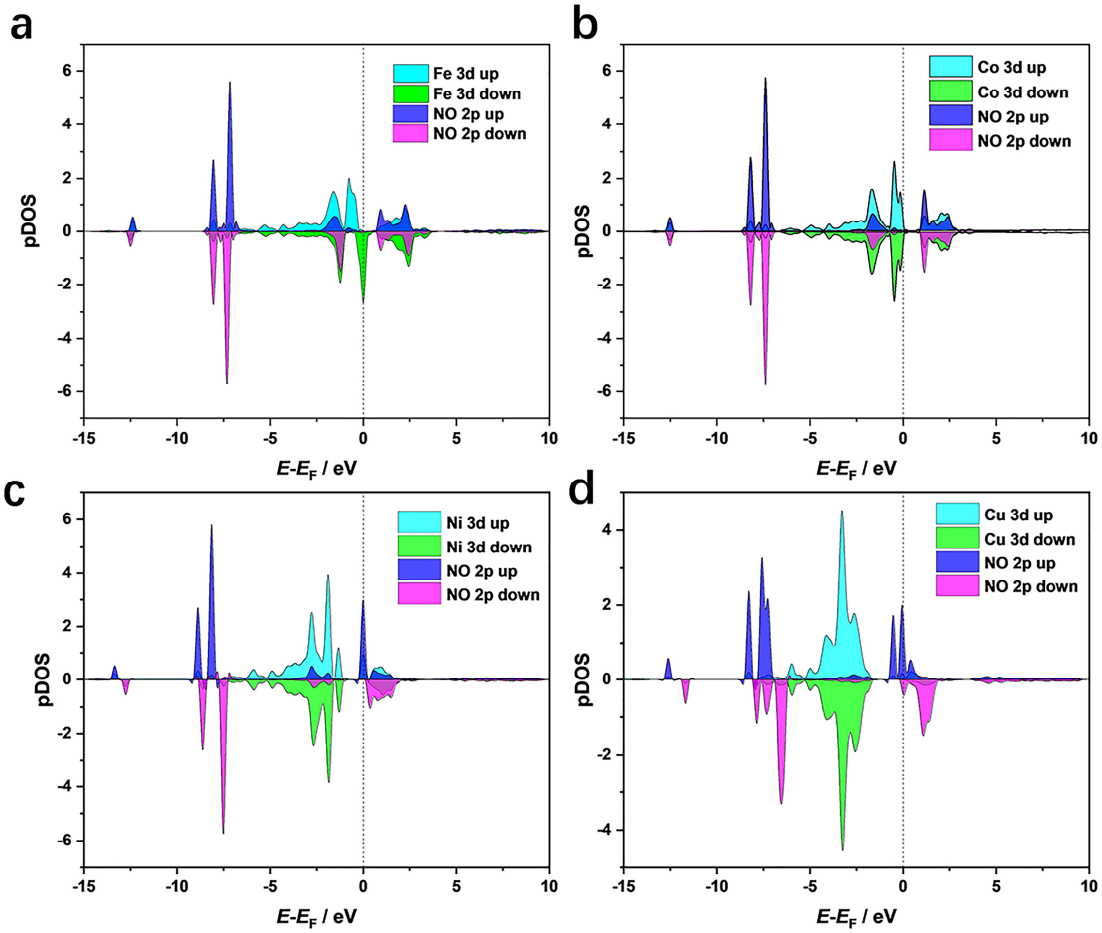

Supplementary Figure 16. Projected density of states (PDOS) of NO adsorbed on Fe-MoS_2 (**a**), Co-MoS_2 (**b**), Ni-MoS_2 (**c**), and Cu-MoS_2 (**d**), respectively. E_F stands for the Fermi level, referring to 0 eV.

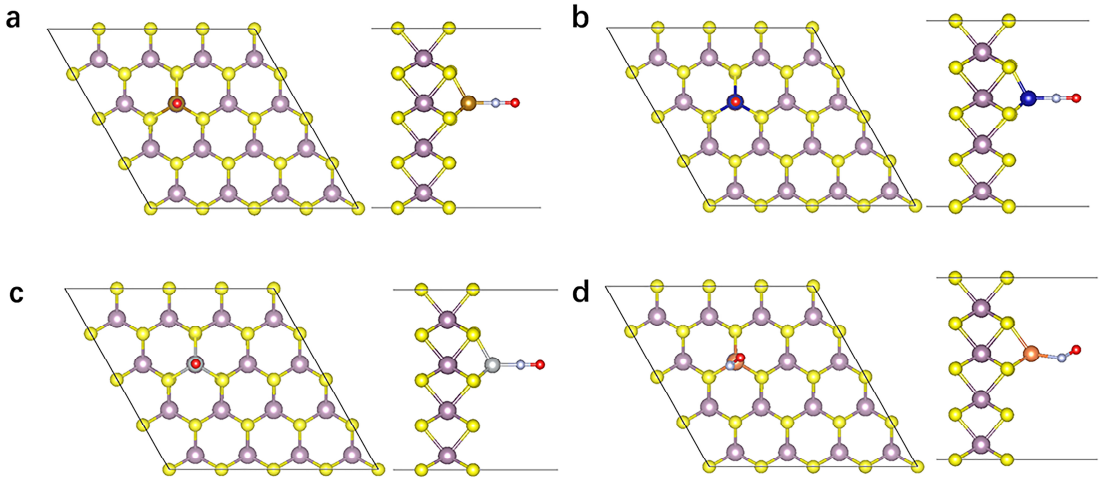

Supplementary Figure 17. Top and side views of the structure of NO adsorbed on Fe-MoS_2 (**a**), Co-MoS_2 (**b**), Ni-MoS_2 (**c**), and Cu-MoS_2 (**d**), respectively. The color code used of the different elements is as follows: Fe (brown), Mo (violet), S (yellow), Co (blue), Cu (orange), Ni (grey), N (light blue), and O (red), respectively.

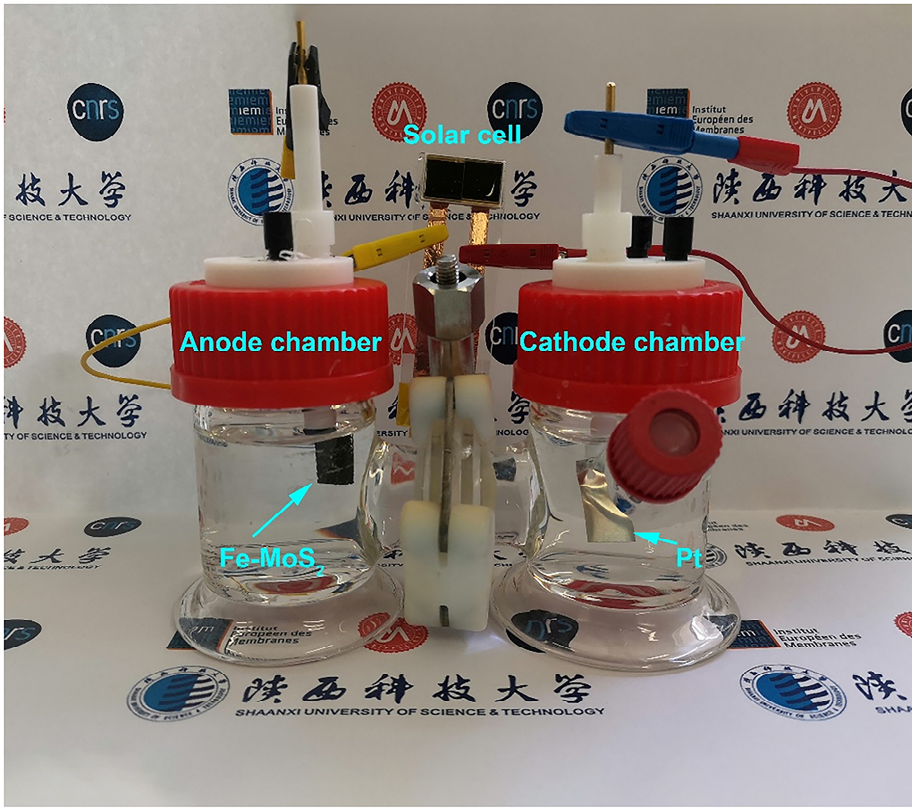

Supplementary Figure 18. Photograph of the 2-electrode H-cell reactor for NO_3RR using Fe-MoS_2 nanosheets and Pt as catalysts for the cathode and anode respectively. The electrolysis reactor is coupled to the external PV-cell.

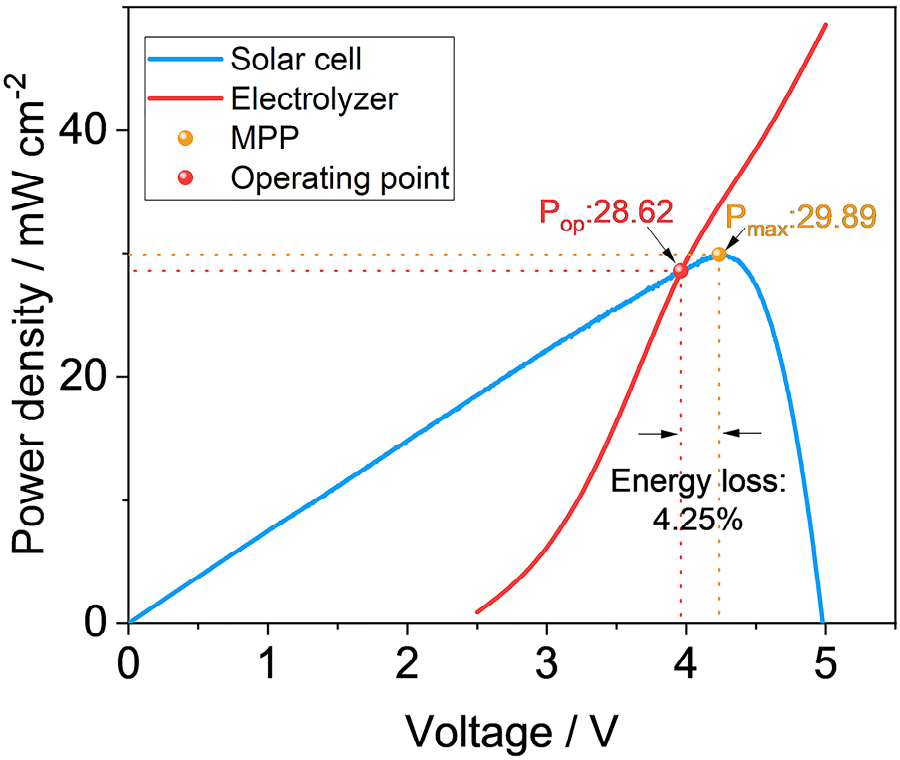

Supplementary Figure 19. The power density of InGaP/GaAs/Ge triple-junction solar cell (area: 2.0 cm^{-2}) under AM 1.5G (100 mW cm^{-2}) (blue line); and the power density of the 2-electrode electrolyzer under different voltages (red line), in which the 2 cm^{-2} of Fe-MoS_2 was used as working electrode.

Supplementary Table 1. Extended X-ray absorption fine structure (EXAFS) fitting parameters at the Fe K-edge for Fe-MoS_2.

Sample	Shell	N [a]	R (Å) [b]	σ^2 (Å^2·10^{-3}) [c]	ΔE_0 (eV) [d]	*R* factor (%)
Fe-MoS_2	Fe-O	2.7	1.97	5.7	-1.5	0.1
	Fe-S	3.5	2.25	5.8	-1.1	
	Fe-O-Fe	0.9	3.02	8.0	-0.8	

[a] *N*: coordination numbers; [b] *R*: bond distance; [c] σ^2: Debye-Waller factors; [d] ΔE_0: the inner potential correction. *R* factor: goodness of fit. S_0^2 was set as 0.85 for Fe-S, which was obtained from the experimental EXAFS fit of reference FeS by fixing S as the known crystallographic value.

Supplementary Table 2. Atomic percent of element (at%) obtained from XPS spectra of MoS_2 and Fe-MoS_2 nanosheets.

Sample	BE(eV) [a]			Atomic % [b]		
	Mo 3d	S 2p	Fe 2p	Mo 3d	S 2p	Fe 2p
MoS_2	229.0/232.3	162.0/163.0	N.F [c]	8.51	21.45	0
Fe-MoS_2-25	229.0/232.2	161.9/163.3	708.3/721.0	7.21	24.92	1.36
Fe-MoS_2-50	229.0/232.3	162.0/163.6	708.2/721.0	8.52	28.44	1.89
Fe-MoS_2-75	229.1/232.3	162.0/163.2	708.3/721.1	9.42	29.54	2.13
Fe-MoS_2-100	229.2/232.5	162.1/163.5	708.3/721.1	8.03	28.67	2.14

[a] The binding energy (BE) was corrected for charging effects, using 284.6 eV as the carbon standard. [b] The atomic percentage determined by XPS spectra. [c] N.F means Not found

346 **Supplementary Table 3**. The concentration of $^{14}NH_3$ and $^{15}NH_3$ detected by NMR
347 and UV using 0.5 M $K^{14}NO_3$ and 0.5 M $K^{15}NO_3$ as electrolyte after 4h reaction at -
348 0.48 V vs.RHE respectively.

Samples	NMR (mM)	UV	Average (mM)
$^{14}NH_3$	10.48	8.77	9.62±1.21
$^{15}NH_3$	5.68	6.52	6.10±0.59

349

Supplementary Table 4. Density functional theory (DFT) calculations of the electronic energies and the associated thermodynamic data associated with the successive steps for the NO_3RR.

Species	E_{DFT} (eV)	E_{ZPE} (eV)	TS (eV)	G (eV)
H_2O (l)	-14.22	0.57	0.57	-14.22
H_2 (g)	-6.96	0.27	0.11	-6.80
NO (g)	-12.28	0.12	0.13	-12.28

Fe-MoS_2

Species	E_{DFT} (eV)	E_{ZPE} (eV)	TS (eV)	G (eV)
slab	-355.01	--	--	-355.01
$*NO_3^-$ [a]	-381.32	0.70	0.27	-380.89
** NO_3^- [b]	-382.83	0.71	0.28	-382.40
$**NO_2$	-375.40	0.27	0.21	-375.34
**NO	-370.38	0.20	0.15	-370.33
**N	-362.54	0.08	0.07	-362.53
**NH	-366.86	0.34	0.12	-366.64
$**NH_2$	-371.57	0.64	0.16	-371.09
$**NH_3$	-375.82	1.02	0.13	-374.94

Co-MoS_2

Species	E_{DFT} (eV)	E_{ZPE} (eV)	TS (eV)	G (eV)
slab	-354.56	--	--	-354.56
$*NO_3^-$	-380.28	0.35	0.20	-380.13
** NO_3^-	-382.02	0.40	0.22	-381.84
$**NO_2$	-374.37	0.27	0.15	-374.25
**NO	-369.70	0.20	0.09	-369.59

**N	-360.71	0.06	0.05	-360.69
**NH	-365.44	0.32	0.13	-365.25
**NH_2	-370.57	0.65	0.14	-370.06
**NH_3	-375.07	1.03	0.19	-374.23

Ni-MoS_2

Species	E_{DFT} (eV)	E_{ZPE} (eV)	TS (eV)	G (eV)
slab	-353.51	--	--	-353.51
*NO_3^-	-379.21	0.36	0.26	-379.11
** NO_3^-	-380.88	0.40	0.24	-380.73
**NO_2	-373.02	0.27	0.22	-372.97
**NO	-367.47	0.17	0.13	-367.43
**N	-358.82	0.05	0.09	-358.87
**NH	-363.98	0.30	0.14	-363.82
**NH_2	-369.19	0.66	0.13	-368.67
**NH_3	-374.34	1.03	0.16	-373.48

Cu-MoS_2

Species	E_{DFT} (eV)	E_{ZPE} (eV)	TS (eV)	G (eV)
slab	-351.00	--	--	-351.00
*NO_3^-	-376.75	0.36	0.20	-376.59
** NO_3^-	-378.18	0.40	0.30	-378.08
**NO_2	-371.51	0.25	0.20	-371.46
**NO	-364.51	0.15	0.09	-364.44
**N	-355.36	0.05	0.11	-355.42
**NH	-361.22	0.31	0.15	-361.07
**NH_2	-367.34	0.65	0.16	-366.85

**NH_3	-371.51	1.03	0.19	-370.67

MoS_2

Species	E_{DFT} (eV)	E_{ZPE} (eV)	TS (eV)	G (eV)
slab	-414.41	--	--	-414.41
*NO_3^-	-441.87	0.36	0.26	-441.78
** NO_3^-	-445.91	0.37	0.17	-445.72
**NO_2	-436.91	0.25	0.16	-436.82
**NO	-430.85	0.17	0.10	-430.77
**N	-423.54	0.08	0.06	-423.52
**NH	-428.13	0.36	0.09	-427.86
**NH_2	-431.84	0.66	0.13	-431.31
**NH_3	-435.29	1.02	0.17	-434.44

[a] * represent physical adsorption;

[b] ** represent chemical adsorption.

Supplementary Table 5. Comparison of the NO_3RR performance with those from other reported electrocatalysts.

Electrocatalyst	Onset potential (V vs. RHE)	Faradaic efficiency (%)	Yield rate	Ref.
Fe-MoS_2	-0.20	~98 ± 8.8 %	0.03 mmol cm^{-2} h^{-1}	This work
Cu/Cu_2O NWAs	-0.20	~95.8%	0.249 mmol cm^{-2} h^{-1}	[20]
$Cu_{50}Ni_{50}$	~0.25	~99%	--	[5]
Copper–molecular solid catalyst	~0.23	~85.9%	0.025 mmol cm^{-2} h^{-1}	[21]
Cu nanosheets	-0.15	99.7%	390.1 μg mg_{Cu}^{-1} h^{-1}	[22]
Titanium	--	82%	--	[23]

Supplementary Table 6. The $E_{ads,NO}$ on various single-atom catalysts.

Catalysts	E_{**NO} (eV)	E_{slab} (eV)	E_{NO} (eV)	$\Delta E_{ads,NO}$ (eV)
Fe-MoS_2	-370.38	-355.01	-12.28	-3.09
Co-MoS_2	-369.70	-354.56	-12.28	-2.86
Ni-MoS_2	-367.47	-353.51	-12.28	-1.68
Cu-MoS_2	-364.51	-351.00	-12.28	-1.23

Supplementary Table 7. Comparison of the NO_3RR performance with those from other reported photocatalysts.

Photocatalyst	Energy efficiency (%)	STA(%)	Yield rate	Ref.
Fe-MoS_2	~21	~3.4 %	30 μmol cm^{-2} h^{-1}	This work
Pd-TiO_2	--	--	26 μmol h^{-1} g^{-1}	[24]
TiO_2	--	--	17 μmol h^{-1} g^{-1}	[25]
NU-1000 supported Fe	--	--	2.9 μmol h^{-1} g^{-1}	[26]

References

1. Huang, L.-Z. et al. Single Fe atoms confined in two-dimensional MoS2 for sulfite activation: A biomimetic approach towards efficient radical generation. *Appl. Catal. B Environ.* **268**, 118459 (2020).

2. Zhang, L. et al. Electrochemical Ammonia Synthesis via Nitrogen Reduction Reaction on a MoS 2 Catalyst: Theoretical and Experimental Studies. *Adv. Mater.* **30**, 1800191 (2018).

3. Yang, J. et al. Ultrahigh-current-density niobium disulfide catalysts for hydrogen evolution. *Nat. Mater.* **18**, 1309–1314 (2019).

4. Li, L. et al. Role of sulfur vacancies and undercoordinated Mo regions in MoS2 nanosheets toward the evolution of hydrogen. *ACS Nano* **13**, 6824–6834 (2019).

5. Wang, Y. et al. Enhanced Nitrate-to-Ammonia Activity on Copper–Nickel Alloys via Tuning of Intermediate Adsorption. *J. Am. Chem. Soc.* **142**, 5702–5708 (2020).

6. Zhu, D. et al. Photo-illuminated diamond as a solid-state source of solvated electrons in water for nitrogen reduction. *Nat. Mater.* **12**, 836–841 (2013).

7. Gurudayal, G. et al. Efficient solar-driven electrochemical CO 2 reduction to hydrocarbons and oxygenates. *Energy Environ. Sci.* **10**, 2222–2230 (2017).

8. Küngas, R. Review—Electrochemical CO 2 Reduction for CO Production: Comparison of Low- and High-Temperature Electrolysis Technologies . *J. Electrochem. Soc.* **167**, 044508 (2020).

9. Chen, Z. et al. Grain-Boundary-Rich Copper for Efficient Solar-Driven

Electrochemical CO 2 Reduction to Ethylene and Ethanol. *J. Am. Chem. Soc.* **142**, 6878–6883 (2020).

10. Kresse, G. et al. Ab initio molecular dynamics for liquid metals. *Phys. Rev. B* **47**, 558–561 (1993).

11. Kresse, G. et al. Ab initio molecular dynamics for open-shell transition metals. *Phys. Rev. B* **48**, 13115–13118 (1993).

12. Yang, T. et al. High-throughput screening of transition metal single atom catalysts anchored on molybdenum disulfide for nitrogen fixation. *Nano Energy* **68**, 104304 (2020).

13. Grimme, S. Semiempirical GGA-type density functional constructed with a long-range dispersion correction. *J. Comput. Chem.* **27**, 1787–1799 (2006).

14. Nørskov, J.K. et al. Origin of the overpotential for oxygen reduction at a fuel-cell cathode. *J. Phys. Chem. B* **108**, 17886–17892 (2004).

15. Ravel, B. et al. ATHENA, ARTEMIS, HEPHAESTUS: Data analysis for X-ray absorption spectroscopy using IFEFFIT. In Journal of Synchrotron Radiation (International Union of Crystallography), pp. 537–541.

16. Koningsberger, D.C. et al. X-ray absorption: principles, applications, techniques of EXAFS, SEXAFS, and XANES.(1988).

17. Rehr, J.J. et al. Theoretical approaches to x-ray absorption fine structure. *Rev. Mod. Phys.* **72**, 621–654 (2000).

18. Bligaard, T. et al. The Brønsted-Evans-Polanyi relation and the volcano curve in heterogeneous catalysis. *J. Catal.* **224**, 206–217 (2004).

19. Medford, A.J. et al. From the Sabatier principle to a predictive theory of transition-metal heterogeneous catalysis. *J. Catal.* **328**, 36–42 (2015).

20. Wang, Y. et al. Unveiling the Activity Origin of a Copper-based Electrocatalyst for Selective Nitrate Reduction to Ammonia. *Angew. Chemie Int. Ed.* **59**, 5350–5354 (2020).

21. Chen, G.-F. et al. Electrochemical reduction of nitrate to ammonia via direct eight-electron transfer using a copper–molecular solid catalyst. *Nat. Energy* **5**, 605–613 (2020).

22. Fu, X. et al. Alternative route for electrochemical ammonia synthesis by reduction of nitrate on copper nanosheets. *Appl. Mater. Today* (2020).

23. McEnaney, J.M. et al. Electrolyte engineering for efficient electrochemical nitrate reduction to ammonia on a titanium electrode. *ACS Sustain. Chem. Eng.* (2020).

24. Walls, J.M. et al. Microwave synthesised Pd–TiO 2 for photocatalytic ammonia production. *RSC Adv.* **9**, 6387–6394 (2019).

25. Hirakawa, H. et al. Selective Nitrate-to-Ammonia Transformation on Surface Defects of Titanium Dioxide Photocatalysts. *ACS Catal.* **7**, 3713–3720 (2017).

26. Choi, H. et al. Vapor-Phase Fabrication and Condensed-Phase Application of a MOF-Node-Supported Iron Thiolate Photocatalyst for Nitrate Conversion to Ammonium. *ACS Appl. Energy Mater.* **2**, 8695–8700 (2019).